Supplementary Materials

Modulation of Large-scale Synoptic Circulation Pattern on Surface Biophysical Environmental variation in the South China Sea

Shuhong Liu [1, 2], Yuanjian Yang[1, 2, 3], Danling Tang[2,*], Hong Yan[3] and Guicai Ning[4]

1 School of Atmospheric Physics, Nanjing University of Information Science & Technology, Nanjing, 210044, China
2 Southern Marine Science and Engineering Guangdong Laboratory (Guangzhou), 511458; Guangdong Key Laboratory of Ocean Remote Sensing, South China Sea Institute of Oceanology, Chinese Academy of Sciences, Guangzhou, 510301, China
3 State Key Laboratory of Loess and Quaternary Geology, Institute of Earth Environment, Chinese Academy of Sciences, Xi'an, 710061, China
4 Institute of Environment, Energy and Sustainability, The Chinese University of Hong Kong, Hong Kong, China

*Corresponding author: Prof. D. Tang (lingzistdl@126.com)

Contents

1. **Text S1: The correction of Two types of noise for the chl-a product of Himawari-8**
2. **Text S2: Ekman pumping and Ekman transport**
3. **Text S3: Determining the number of synoptic patterns**
4. **Tables and captions**
5. **Figures and captions**
6. **Reference**

1. Text S1: The correction of Two types of noise for the chl-a product of Himawari-8

The correction of Two types of noise for the chl-a product of Himawari-8 was given as followings: First, Figure S1a shows the horizontal distribution of chl-a without any noise subtractions. It can be seen that there are two noises, one is a striping noise with an interval of about 5°, and the other is a spikelike noise. Then deal with them according to the noise removal method in Iwasaki [1]. Since MODIS can also provide monthly chl-a products without striping noise, we fit the monthly chl-a of Himawari-8 to that of MODIS by using the regression lines at each pixel. This study calculated the regression lines between the monthly chl-a of Himawari-8 and those of MODIS from August 2015 to December 2018 at each pixel. The horizontal distribution of chl-a after the MODIS fitting is shown in Figure S1b, basically the striping noise is removed. Finally, median filtering is used to reduce spikelike noise. The median filtering converts the value of a certain pixel to the median of 9 pixels. That is, with the target pixel as the center, the eight surrounding pixel values are sorted in order of magnitude, and their median value is selected as the value of the target pixel. In this way, the two types of noise are greatly reduced (Figure S1c).

2. Text S2: Ekman pumping and Ekman transport

This research requires the calculation of the upwelling (*upw*) caused by Ekman pumping. Price [2] proposed the Ekman pumping formula as follows:

$$upw = \nabla \times (\boldsymbol{\tau}/\rho f), \tag{1}$$

where f is the Coriolis parameter, ρ is the seawater density (1020kg m^{-3}), and $\boldsymbol{\tau}$ is the wind stress vector, which can be calculated as follows:

$$\boldsymbol{\tau} = \rho_a C_D |\mathbf{U_{10}}| \mathbf{U_{10}}; \tag{2}$$

$$C_D = \begin{cases} (4 - 0.6|\mathbf{U_{10}}|) \times 10^{-3} & for\ |\mathbf{U_{10}}| < 5\ m\ s^{-1}; \\ (0.737 + 0.0525|\mathbf{U_{10}}|) \times 10^{-3} & for\ 5\ m\ s^{-1} \le |\mathbf{U_{10}}| < 25 m\ s^{-1}. \\ 2.05 \times 10^{-3} & for\ |\mathbf{U_{10}}| \ge 25\ m\ s^{-1} \end{cases} \tag{3}$$

where ρ_a is the air density (1.26 kg m^{-3}), C_D is the drag coefficient [3,4], and $\mathbf{U_{10}}$ is the 10-m wind vector.

Ekman's assumption that the frictional force acted only in the surface layer allowed him to estimate the volume transport within the layer by integrating from the sea surface. The Ekman transport relation is given by [5]:

$$M_x = \frac{\tau_y}{\rho f};\ M_y = -\frac{\tau_x}{\rho f}\ , \tag{4}$$

where M_x is the eastward component of Ekman transport and M_y is the northward component.

3. Text S3: Determining the number of synoptic patterns

The explained cluster variance (ECV) ranging from 0 to 1is selected to assess the performance of synoptic classification and to determine the number of classes [6,7]. ECV is defined as:

$$ECV = 1 - \frac{WS}{TS} \tag{5}$$

Where *WS* is the sum of squares within synoptic patterns, and *TS* is the total of sum of squares:

$$WS = \sum_{j=1}^{k} \sum_{i \in C_j} D^2{}_{(Y_i, \overline{Y_j})} \tag{6}$$

$$TS = \sum_{i=1}^{n} \sum_{l=1}^{m} (Y_{il}, \overline{Y_l})^2 \tag{7}$$

where k is synoptic patterns number, C_j is the pattern j, and the squared Euclidean distance $D^2{}_{(Y_i, \overline{Y_j})}$ between an element and its centroid is defined as:

$$D^2{}_{(Y_i, \overline{Y_j})} = \sum_{l=1}^{m} \left(Y_{il}, \overline{Y_{jl}}\right)^2 \tag{8}$$

where l is the time step (l=1, 2, …, m), Y_{il} is the respective data point, $\overline{Y_{jl}}$ is the estimate of the mean value for synoptic pattern j, $\overline{Y_l}$ is the estimate of the total mean.

Then, the synoptic patterns number k can be determined by the increment of the *ECV* value [8]:

$$\Delta ECV = ECV_k - ECV_{k-1} \tag{9}$$

The number of synoptic patterns k is finally determined when the ΔECV reaches the highest value, which suggests that the classification performance is improved substantially and tends to be stable [8].

4. Tables and captions

Table S1. The typhoons in SCS and their impacts periods during summertime from 2015-2018.

Year	Typhoon name	Transit periods	Total impact periods
2015	LINFA	7.4-7.10	7.4-7.17
2016	MIRINAE	7.25-7.28	7.25-8.4
	NIDA	7.31-8.2	7.31-8.5
	NIANMU*	8.18-8.19	8.18-8.26
2017	MERBOK*	6.11-6.13	6.11-6.16
	TALAS*	7.15-7.17	7.15-7.20
	SONCA*	7.21-7.25	7.21-8.1
	ROKE*	7.21-7.23	7.21-7.31
	HAITANG*	7.28-7.31	7.28-8.3
	HATO	8.21-8.24	8.21-8.31
	PAKHAR	8.25-8.27	8.25-8.31
2018	EWINIAR*	6.5-6.9	6.5-6.16
	SON-TINH*	7.17-7.25	7.17-8.1
	BEBINCA	8.12-8.17	8.12-8.21

Table S2. The total days for each type.

	Type 1	Type 2	Type 3	Type 4
June	87	2	1	0
July	28	62	23	10
August	21	53	28	22
Summer	136	117	52	32

Table S3. The days for each type after removing the typhoon impact days.

	Type 1	Type 2	Type 3	Type 4
June	69	2	1	0
July	15	38	16	1
August	12	50	12	11
Summer	96	90	29	12

5. Figures and Captions

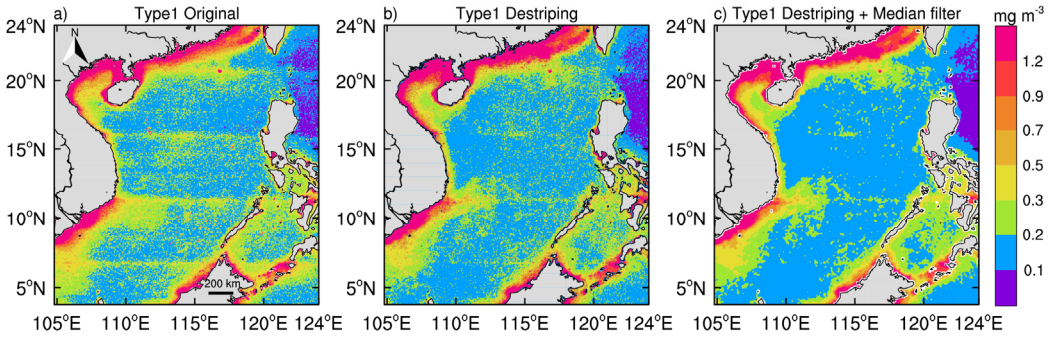


Figure S1 (a) Type 1 chl-a concentration of Himawari 8; (b) Same as (a) but with noise removed by destriping procedure; (c) Same as (a) but with noise removed by median filter and destriping procedure.

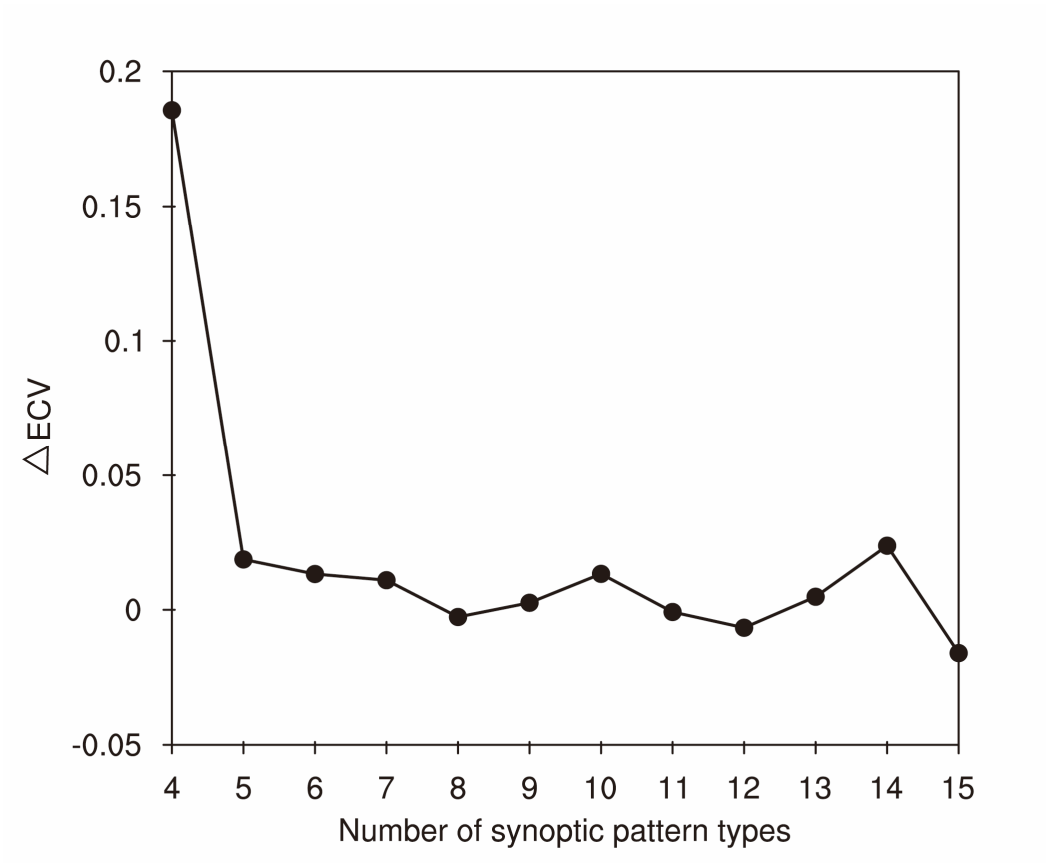


Figure S2 Changes of *ΔECV* with different numbers of classified synoptic patterns.

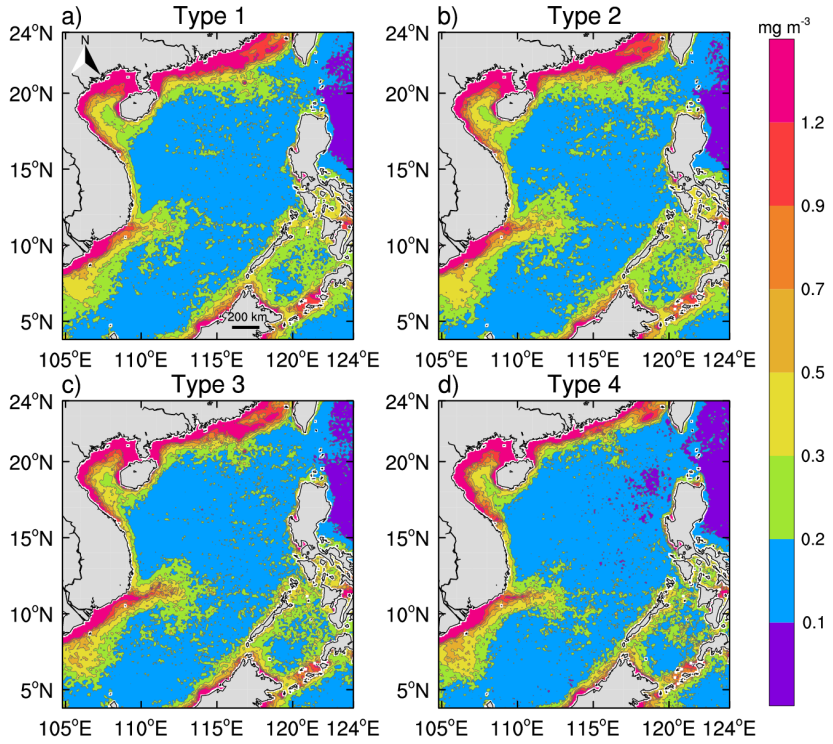


Figure S3. Mean chl-a concentration in four synoptic types: (a) Type 1; (b) Type 2; (c) Type 3; (d) Type 4.

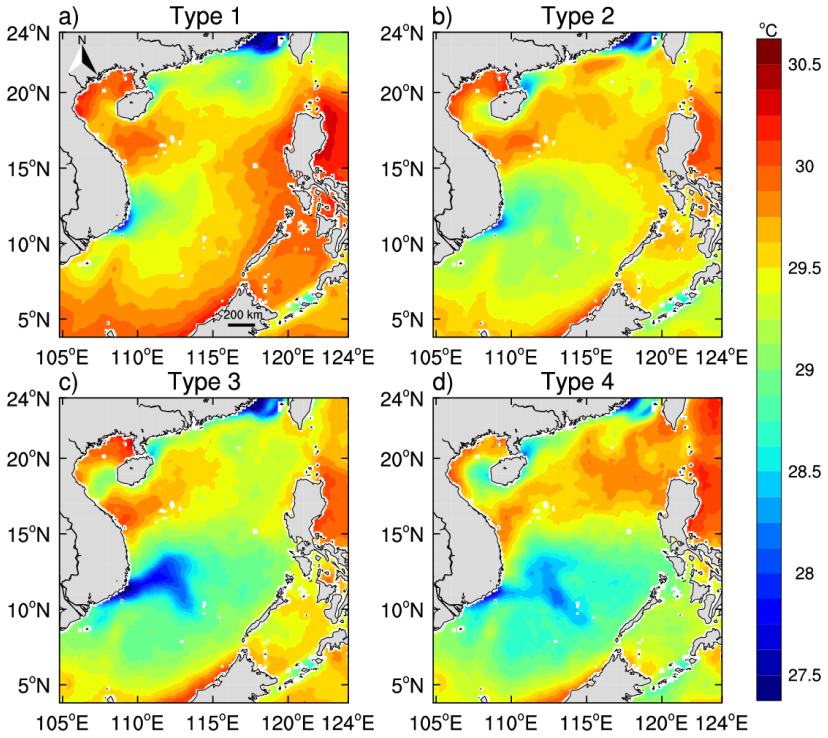


Figure S4. Mean SST in four synoptic types: (a) Type 1; (b) Type 2; (c) Type 3; (d) Type 4.

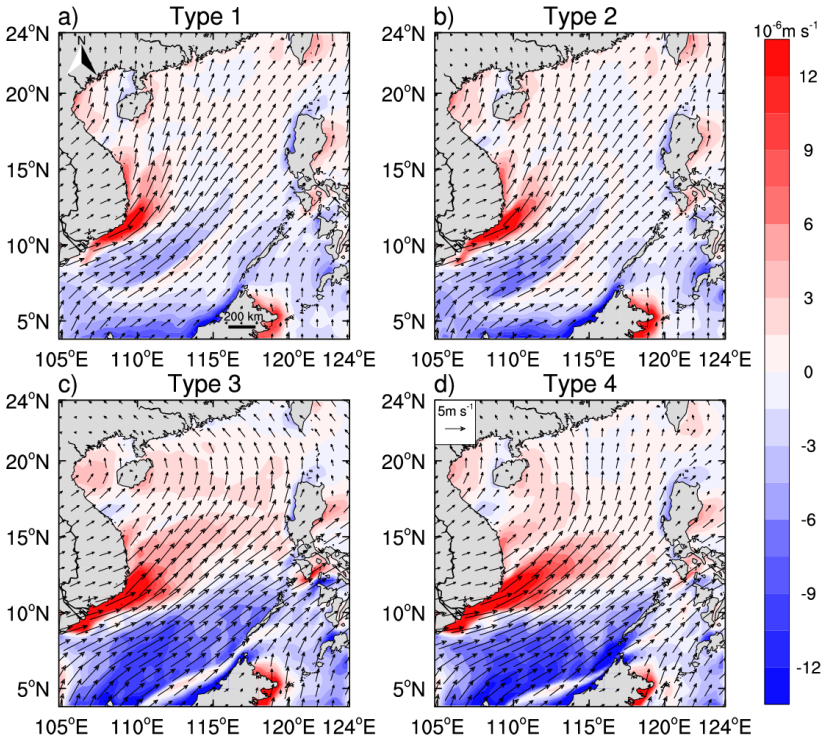


Figure S5. Mean wind fields at 10 m (arrows) and the Ekman pumping velocity (shaded, positive value is upwelling) in four synoptic types: (a) Type 1; (b) Type 2; (c) Type 3; (d) Type 4.

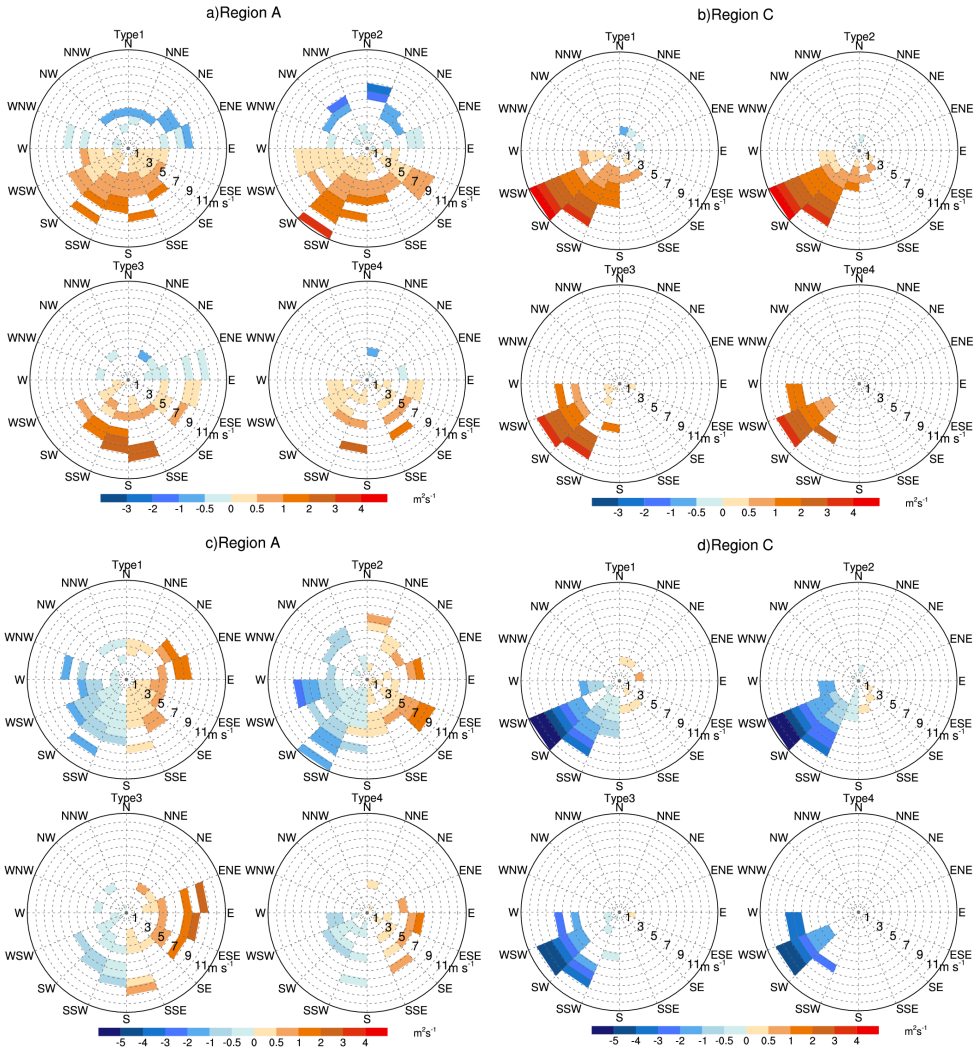


Figure S6. Roses of the Wind (m s^{-1}) and Ekman transport (shaded, m^2 s^{-1}) in X (eastward is positive) and Y (northward is positive) directions in four weather patterns in the coastal regions shown in the black box in Figure 3d (Regions A and C). (a) Ekman transport in X direction in Region A; (b) Ekman transport in X direction in Region C; (c) Ekman transport in Y direction in Region A; (d) Ekman transport in Y direction in Region C.

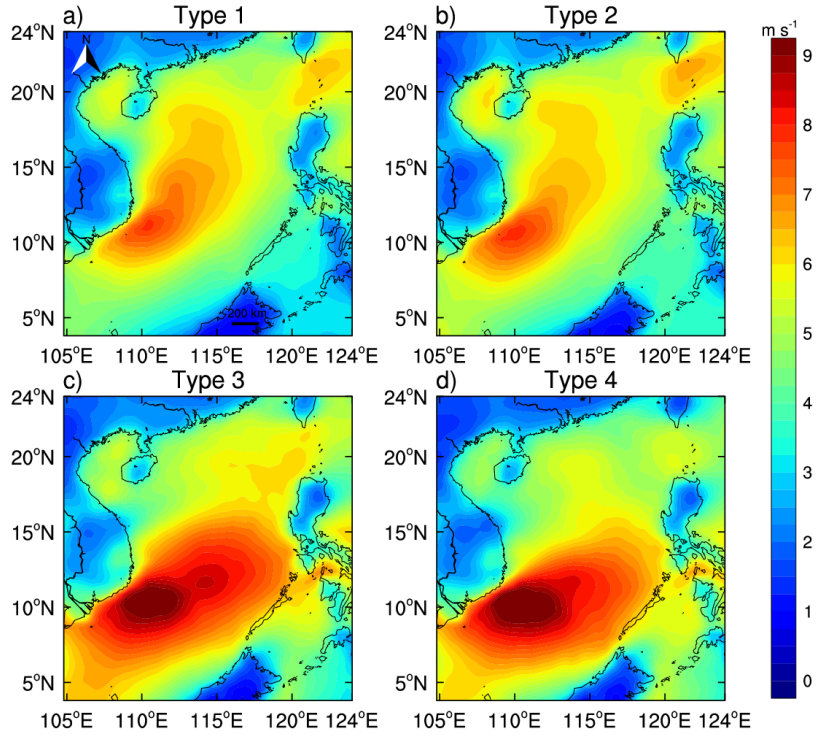


Figure S7. Mean wind speed at 10 m (shaded, m s^{-1}) in four synoptic types: (a) Type 1; (b) Type 2; (c) Type 3; (d) Type 4.

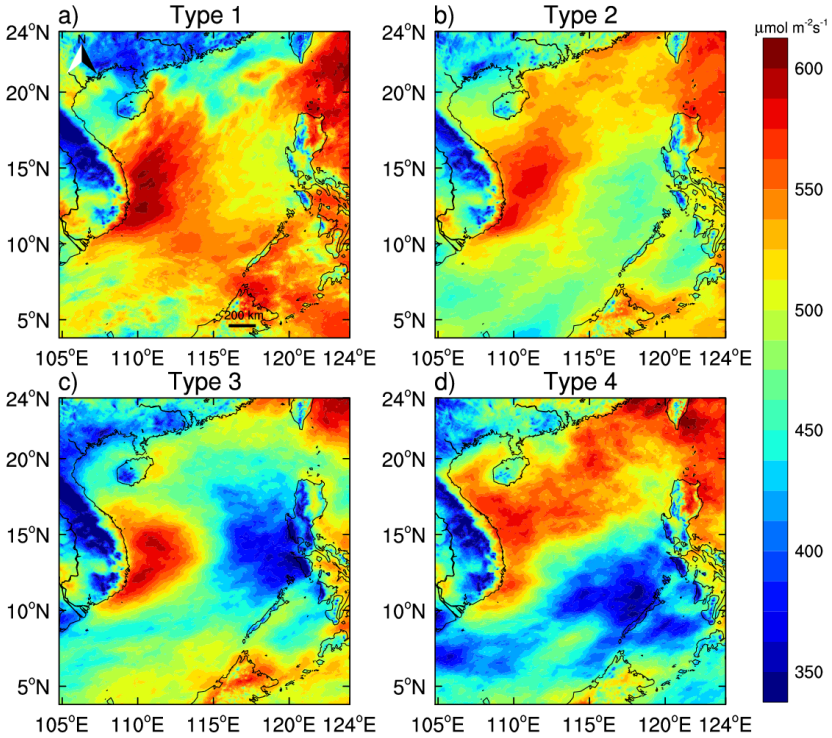


Figure S8. Mean PAR (shaded, µmol $m^{-2}s^{-1}$) in four synoptic types: (a) Type 1; (b) Type 2; (c) Type 3; (d) Type 4.

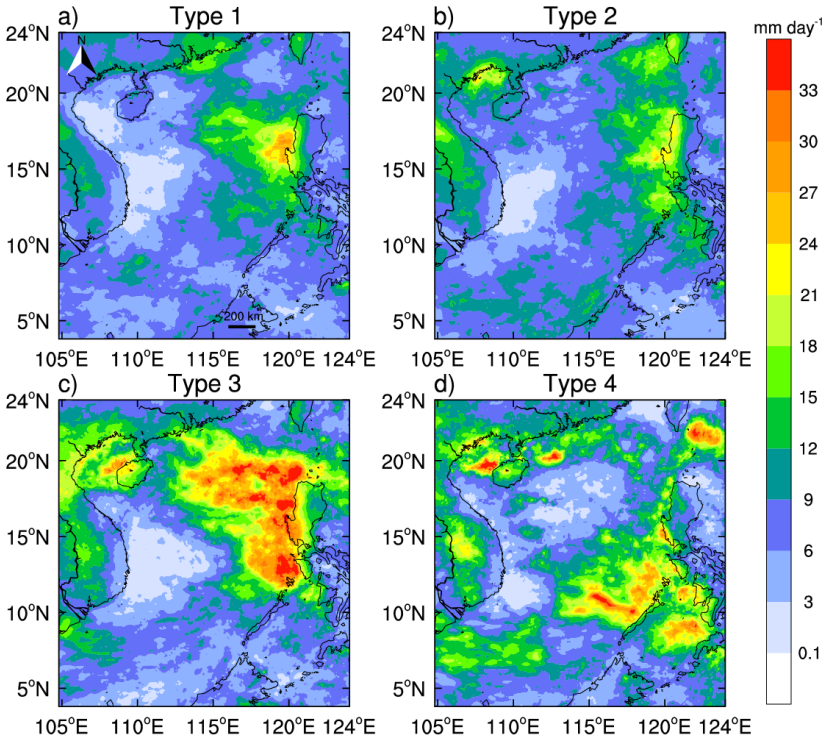


Figure S9. Mean rainfall (shaded, mm day^{-1}) in four synoptic types: (a) Type 1; (b) Type 2; (c) Type 3; (d) Type 4.

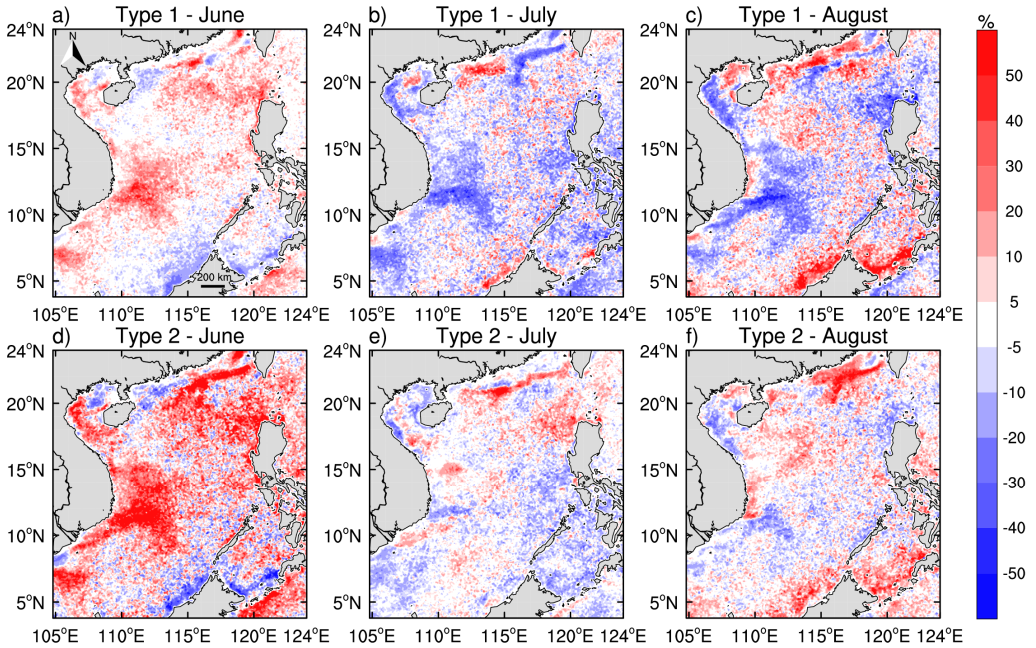


Figure S10. Deviation percentage of chl-a concentration in Type 1 and Type 2 in summer each month. (a-c) The deviation percentage of type 1 from June, July, and August respectively; (d-f) the deviation percentage of type 2 from June, July, and August respectively.

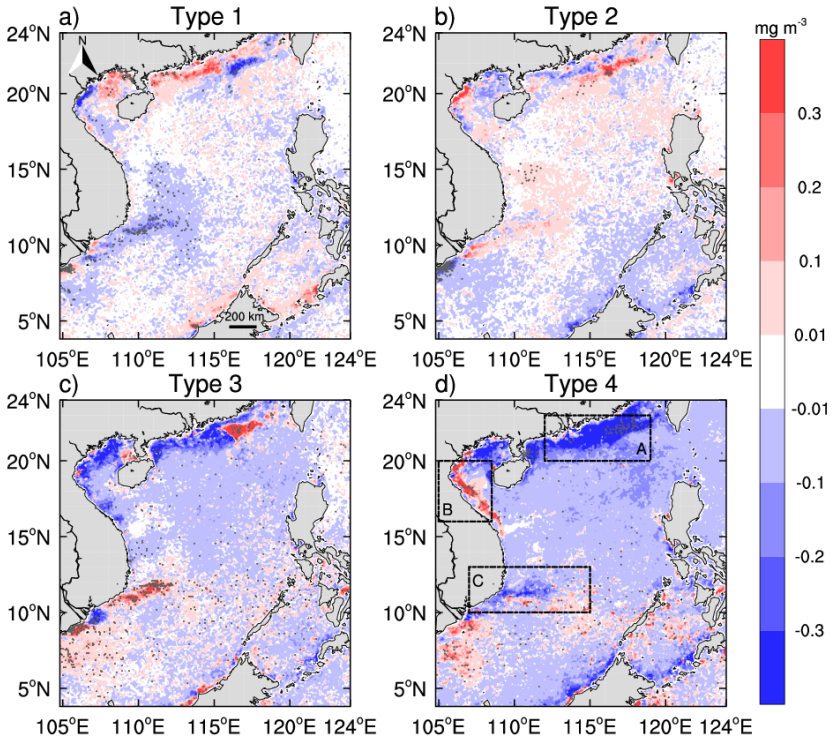


Figure S11. Chl-a concentration anomaly in four synoptic types which remove typhoon effects (the gray dots cover areas with significant differences): (a) Type 1; (b) Type 2; (c) Type 3; (d) Type 4.

6. Reference：

1. Iwasaki, S. Daily Variation of Chlorophyll-A Concentration Increased by Typhoon Activity. *Remote Sens.* **2020**, *12*, 1259, doi: 10.3390/rs12081259.
2. Price, J.F. Upper ocean response to a hurricane. *J. Phys. Oceanogr.* **1981**, *11*, 153–175, doi: 10.1175/1520-0485(1981)011<0153:UORTAH>2.0.CO;2.
3. Jaimes, B.; Shay, L.K. Enhanced wind-driven downwelling flow in warm oceanic eddy features during the intensification of Tropical Cyclone Isaac (2012): Observations and theory. *J. Phys. Oceanogr.* **2015**, *45*, 1667–1689, doi: 10.1175/JPO-D-14-0176.1
4. Powell, M.D.; Vickery, P.J.; Reinhold, T.A., Reduced drag coefficient for high wind speeds in tropical cyclones. *Nature* **2003**, *422*, 279–283, doi: 10.1038/nature01481.
5. Chereskin, T.K.; Price, J.F. Ekman Transport and Pumping. In *Encyclopedia of Ocean Sciences*, 1st ed.; Steele, J.H.; Academic Press: Cambridge, USA, 2001, 809–815, doi: 10.1016/B978-012374473-9.00155-7.
6. Hoffmann, P.; Heinke SchlüNzen, K. Weather pattern classification to represent the urban heat island in present and future climate. *J. Appl. Meteorol. Clim.* **2013**, *52*, 2699–2714, doi: 10.1175/JAMC-D-12-065.1.
7. Philipp, A.; Beck, C.; Esteban, P.; Krennert, T.; Lochbihler, K.; Spyros, P.; Pianko-kluczynska, K.; Post, P.; Alvarez, R.; Spekat, A.; Streicher, F. Cost733 user guide. Available online: https://www.researchgate.net/publication/269335894_COST733CLASS_v12_User_guide (accessed on 10 August 2021).
8. Ning, G.; Yim, S.H.L.; Wang, S.; Duan, B.; Nie, C.; Yang, X.; Wang, J.; Shang, K. Synergistic effects of synoptic weather patterns and topography on air quality: a case of the Sichuan Basin of China. *Clim. Dynam.* **2019**, *53*, 6729–6744, doi: 10.1007/s00382-019-04954-3.